The Astrophysical Journal, 976:249 (10pp), 2024 December 1 https://doi.org/10.3847/1538-4357/ad8912

The Magnetic Field in Quiescent Star-forming Filament G16.96+0.27

Qi-Lao Gu (顾琦烙)[1], Tie Liu (刘铁)[1], Zhi-Qiang Shen (沈志强)[1], Sihan Jiao (焦斯汗)[2], Julien Montillaud[3], Mika Juvela[4], Xing Lu (吕行)[1], Chang Won Lee[5,6], Junhao Liu (刘峻豪)[7], Pak Shing Li[1], Xunchuan Liu (刘训川)[1], Doug Johnstone[8,9], Woojin Kwon[10,11,12], Kee-Tae Kim[5,6], Ken'ichi Tatematsu[13,14], Patricio Sanhueza[7,14], Isabelle Ristorcelli[15], Patrick Koch[16], Qizhou Zhang[17], Kate Pattle[18], Naomi Hirano[16], Dana Alina[19,20], and James Di Francesco[21,22]

[1] Shanghai Astronomical Observatory, Chinese Academy of Sciences, No.80 Nandan Road, Xuhui, Shanghai 200030, People's Republic of China; qlgu@shao.ac.cn, liutie@shao.ac.cn, zshen@shao.ac.cn
[2] National Astronomical Observatories, Chinese Academy of Sciences, A20 Datun Road, Chaoyang, Beijing 100101, People's Republic of China
[3] Université de Franche-Comté, CNRS, Institut UTINAM, OSU THETA, F-25000 Besançon, France
[4] Department of Physics, PO Box 64, FI-00014, University of Helsinki, Finland
[5] Korea Astronomy and Space Science Institute, 776 Daedeokdae-ro, Yuseong-gu, Daejeon 34055, Republic of Korea
[6] University of Science and Technology, Korea, 217 Gajeong-ro, Yuseong-gu, Daejeon 34113, Republic of Korea
[7] National Astronomical Observatory of Japan, 2-21-1 Osawa, Mitaka, Tokyo, 181-8588, Japan
[8] NRC Herzberg Astronomy and Astrophysics, 5071 West Saanich Road, Victoria, BC, V9E 2E7, Canada
[9] Department of Physics and Astronomy, University of Victoria, Victoria, BC, V8P 5C2, Canada
[10] Department of Earth Science Education, Seoul National University, 1 Gwanak-ro, Gwanak-gu, Seoul 08826, Republic of Korea
[11] SNU Astronomy Research Center, Seoul National University, 1 Gwanak-ro, Gwanak-gu, Seoul 08826, Republic of Korea
[12] The Center for Educational Research, Seoul National University, 1 Gwanak-ro, Gwanak-gu, Seoul 08826, Republic of Korea
[13] Nobeyama Radio Observatory, National Astronomical Observatory of Japan, National Institutes of Natural Sciences Nobeyama, Minamimaki, Minamisaku, Nagano 384-1305, Japan
[14] Astronomical Science Program, Graduate Institute for Advanced Studies, SOKENDAI 2-21-1 Osawa, Mitaka, Tokyo 181-8588, Japan
[15] IRAP, Université de Toulouse, CNRS, 9 Avenue du Colonel Roche, BP 44346, 31028 Toulouse Cedex 4, France
[16] Academia Sinica Institute of Astronomy and Astrophysics, No. 1, Section 4, Roosevelt Road, Taipei 10617, Taiwan (R.O.C.)
[17] Center for Astrophysics | Harvard & Smithsonian, 60 Garden Street, Cambridge, MA 02138, USA
[18] Department of Physics and Astronomy, University College London, Gower Street, London WC1E 6BT, UK
[19] Department of Physics, School of Science and Technology, Nazarbayev University, Astana 010000, Kazakhstan
[20] IRAP, Université de Toulouse CNRS, UPS, CNES, F-31400 Toulouse, France
[21] Department of Physics and Astronomy, University of Victoria, Victoria, BC, V8W 2Y2, Canada
[22] 2 NRC Herzberg Astronomy and Astrophysics, 5071 West Saanich Road, Victoria, BC, V9E 2E7, Canada
Received 2024 August 28; revised 2024 October 18; accepted 2024 October 18; published 2024 November 27

Abstract

We present 850 μm thermal dust polarization observations with a resolution of 14.″4 (∼0.13 pc) toward an infrared dark cloud G16.96+0.27 using James Clerk Maxwell Telescope/POL-2. The average magnetic field orientation, which roughly agrees with the larger-scale magnetic field orientation traced by the Planck 353 GHz data, is approximately perpendicular to the filament structure. The estimated plane-of-sky magnetic field strength is ∼96 μG and ∼60 μG using two variants of the Davis–Chandrasekhar–Fermi methods. We calculate the virial and magnetic critical parameters to evaluate the relative importance of gravity, the magnetic field, and turbulence. The magnetic field and turbulence are both weaker than gravity, but magnetic fields and turbulence together are equal to gravity, suggesting that G16.96+0.27 is in a quasi-equilibrium state. The alignment between the magnetic field and cloud is found to have a trend moving away from perpendicularity in the dense regions, which may serve as a tracer of potential fragmentation in such quiescent filaments.

Unified Astronomy Thesaurus concepts: Magnetic fields (994); Star formation (1569); Molecular clouds (1072); Infrared dark clouds (787); Interstellar filaments (842)

1. Introduction

Filaments are ubiquitous in the interstellar medium (e.g., P. C. Myers 2009; P. André et al. 2010; D. Arzoumanian et al. 2011) with chains of dense cores embedded in them (e.g., Q. Zhang et al. 2009; P. André et al. 2014; V. Könyves et al. 2015; M. Tafalla & A. Hacar 2015; K. Morii et al. 2023), indicating that the filamentary structure might be an important stage in the star formation process (H. B. Liu et al. 2012; X. Lu et al. 2018). The details regarding how filaments fragment into dense prestellar cores and further evolve to form protostars are still under debate. Specifically, the role that the magnetic field plays during this process remains far from being fully understood (R. M. Crutcher 2012; H. B. Li et al. 2014; K. Pattle et al. 2023).

Recent state-of-the-art ideal magnetohydrodynamic simulations of large-scale filamentary cloud formation and evolution (e.g., P. S. Li & R. I. Klein 2019) suggest that a strong magnetic field perpendicular to the filament can support the filamentary structure and guide gas flow along the field onto the main cloud. Observationally, H.-B. Li et al. (2015) found that the magnetic field orientation does not change much over the ∼100 to ∼0.01 pc scale in the filamentary cloud NGC 6334, suggesting self-similar fragmentation regulated by the magnetic field. Within nearby Gould Belt clouds (with distances smaller than 500 pc), the parallel-to-perpendicular trend of cloud–field alignment (the offset between the magnetic field orientation

and the molecular cloud long axis) with increasing density indicates that these clouds may have formed from the accumulation of material along the field lines (Planck Collaboration Int. XXXV et al. 2016). With high-resolution submillimeter polarization observations, T. Liu et al. (2018a) found that, in the massive infrared dark cloud (IRDC) G35.39-0.33, the magnetic field is roughly perpendicular to the densest part of the main filament but tends to be parallel with the gas structure in more diffuse regions. A. Soam et al. (2019) and Y.-W. Tang et al. (2019) found that the magnetic field lines are more pinched by gravitational collapse at the core scale in the more evolved filamentary IRDC G34.42+0.24, where ultra-compact H II regions have formed. T.-C. Ching et al. (2022) reported that a strong magnetic field shapes the main filament and subfilaments of the DR21 region. These results align with the simulations, suggesting that the magnetic field is dynamically important in the star formation process. However, active star formation has already occurred in these filamentary clouds, and feedback from star formation may have changed the initial magnetic field. Therefore, observations of more quiescent clouds are required to investigate the role of the magnetic field in core formation inside filaments.

G16.96+0.27 is one of the brightest filaments in the James Clerk Maxwell Telescope (JCMT) SCOPE survey (T. Liu et al. 2018b) and is located at a distance of 1.87 kpc, embedded with few protostellar and starless cores (G. Kim et al. 2020; E. Mannfors et al. 2021; K. Tatematsu et al. 2021). As shown in the upper panel of Figure 1, G16.96+0.27 has a simple filamentary structure and is dark at the infrared wavelength, so it has not been illuminated by protostars in the infrared band, suggesting it is a quiescent filament at the very early stage of the star formation process. This makes G16.96+0.27 an ideal target to study the magnetic field at the early stage of star formation. Here, we use our 850 μm JCMT/POL-2 thermal dust polarization observations toward G16.96+0.27 to investigate the properties of the magnetic field inside a quiescent IRDC.

This paper is organized as follows: in Section 2, we present our JCMT/POL-2 850 μm observations; in Section 3, we show the results from our observations and calculate the magnetic field strength; in Section 4, we discuss the equilibrium state and multiscale cloud–field alignment; and we provide a summary in Section 5.

2. Observations

G16.96+0.27 was observed 19 times from 2020 August to 2020 October (project code: M20BP043; PI: Tie Liu) using SCUBA-2/POL-2 DAISY mapping mode (W. S. Holland et al. 2013; P. Friberg et al. 2016, 2018) under Band 2 weather conditions ($0.05 < \tau_{225} < 0.08$, where τ_{225} is the atmospheric opacity at 225 GHz), with a total integration time of ~12.8 hr. The effective beam size is 14.″4 at 850 μm (S. Mairs et al. 2021), corresponding to ~0.13 pc at a distance of 1.87 kpc.

The raw data were reduced using the pol2map routine of the STARLINK (M. J. Currie et al. 2014) package, SMURF (E. L. Chapin et al. 2013) with the 2019 August instrumental model,[23] following the same procedures as described in Q.-L. Gu et al. (2024). The final Stokes *I*, *Q*, and *U* maps are in units of pW with a pixel size of 4″, and are converted into the unit of Jy beam^{-1} by applying the 850 μm flux conversion factor of 668 Jy beam^{-1} pW^{-1} (S. Mairs et al. 2021). For the following analysis, we regrid these maps to a pixel size of 8″ for a balance of good signal-to-noise ratio (S/N) level and enough data points. The rms noise levels of the background regions are ~5.3 mJy beam^{-1} in the *I* map and ~4.0 mJy beam^{-1} in the *Q* and *U* maps. The polarization information catalog is created simultaneously from these Stokes maps following the procedures described in Appendix A. Figures 1(b) and (c) show the final *Q* and *U* maps; (a) shows the final *I* map that is combined with Planck 353 GHz flux via the J-comb algorithm (S. Jiao et al. 2022) as described in Appendix B.

3. Results

3.1. Dust Polarization Properties and Magnetic Field Morphology

The projected plane-of-sky (POS) magnetic field orientations are derived by rotating the observed polarization pseudovectors by 90°, based on the grain alignment assumption that the shortest axis of dust grains tends to align with the local magnetic field (A. Lazarian 2003). The polarization pseudovectors are selected by criteria of $I/\delta_I \geqslant 10$, $PI/\delta_{PI} \geqslant 3$, and $\delta_p \leqslant 5\%$, where δ_I is the uncertainty of Stokes *I*, *PI* and δ_{PI} are the debiased polarized intensity and the corresponding uncertainty, and δ_p is the uncertainty of the polarization fraction. The inferred magnetic field orientations are shown in Figure 2 (a) overlaid on the column density ($N(H_2)$) map, which is generated from level 2.5 processed archival Herschel images by the J-comb algorithm, as described in Appendix B (S. Jiao et al. 2022). The magnetic field is roughly perpendicular to the main filament structure with an average orientation of $60 \pm 20°$[24] (Figure 2(c)).

Figure 2(d) shows a decreasing polarization fraction trend with increasing initial dust emission intensity fitted with a power-law index of -0.73 ± 0.04. Figure 2(e) exhibits the distribution of the polarization fraction, which peaks at ~6.5% with a tail extending to ~15%–25%. The average and median of polarization fractions are $7.8 \pm 3.6\%$ and 7.0%.

As shown in Figure 2(a), the magnetic field is roughly perpendicular to the filament structure. In general, the small-scale (14.″4, ~0.13 pc) magnetic field traced by POL-2 agrees with the large-scale (4.′8, ~2.6 pc) magnetic field traced by Planck, showing similar average orientations, $60 \pm 20°$ (POL-2) and $43 \pm 5°$ (Planck). However, in the center of the filament, the small-scale magnetic field shows a ~45° difference from the large-scale one, suggesting the magnetic field orientation varies with increasing $N(H_2)$, which may reflect the effects from gravity and turbulence (see Section 4 for further discussions).

3.2. The Magnetic Field Strength

Before calculating the magnetic field strength, we estimate the gas density (ρ) and line-of-sight nonthermal turbulent velocity dispersion (σ_v). As shown in Figures 2((a)–(b)), we choose three cross sections to apply the Gaussian fit of $N(H_2)$ profiles, and the average half maximum $N(H_2)$ is $(2.38 \pm 0.17) \times 10^{22}$ cm^{-2} with an average FWHM

[23] The details can be found at https://www.eaobservatory.org/jcmt/2019/08/new-ip-models-for-pol2-data/.

[24] All position angles shown in this paper follow the IAU-recommended convention of measuring angles from the north toward the east.

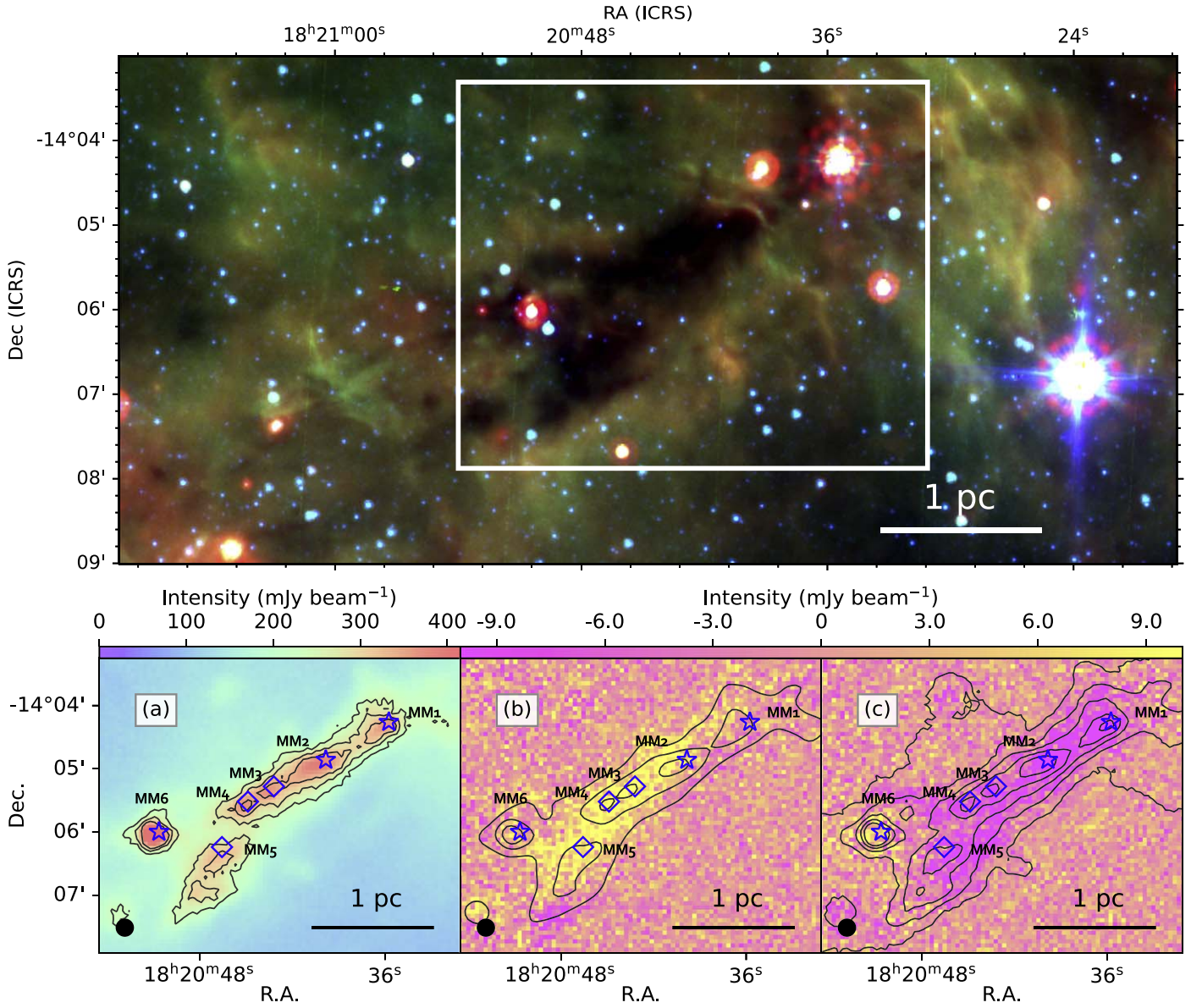

Figure 1. Upper: Spitzer infrared pseudo-color map toward G16.96+0.27 (Red: 24 μm; Green: 8 μm; Blue: 5.8 μm). A 1 pc scale bar is shown in the lower-right corner. The white box marks the region of the lower panels. Lower (a–c): JCMT/POL-2 850 μm Stokes *I*, *Q*, and *U* maps of G16.96+0.27, and the Stokes *I* shown here is a combination of SCUBA-2 850 μm and deconvolved Planck 353 GHz data using the J-comb algorithm (S. Jiao et al. 2022) considering the large-scale flux. Color bars are shown on the top of the lower panels. Details can be found in Appendix B. MM1 to MM6 mark the possible fragments observed at the resolution of $14\farcs4$; star and diamond symbols represent protostellar and starless cores, respectively. Beams and the 1 pc scale bars are shown in the left and right corners, respectively. Contours in (a) show the intensity of 450 μm Stokes *I* at levels of [240, 480, 720] mJy beam^{-1} with an average rms noise level of 44 mJy beam^{-1}. The rms noise of the 450 μm Stokes *Q* and *U* maps is ~41 mJy beam^{-1}, which is not good enough for effective utilization, except in this figure; we do not show any other 450 μm results in this paper, and hereafter *I* , *Q,* and *U* refer to 850 μm data only. Contours in (b) show the column density generated from the Herschel data by the J-comb algorithm (S. Jiao et al. 2022) at levels of [2.22, 3.22, 4.22] $\times 10^{22}$ cm^{-2}. Contours in (c) show the intensity of combined 850 μm Stokes *I* using the J-comb algorithm at levels of [150, 200, 250, 300, 350] mJy beam^{-1} with an average rms noise level of 5.3 mJy beam^{-1}.

~0.46 ± 0.06 pc. Most of the magnetic field segments are inside the contour of $N(H_2) \sim 2.38 \times 10^{22}$ cm^{-2}. Thus, we estimate the mass and ρ using the $N(H_2)$ map by assuming the filament within the 2.38×10^{22} cm^{-2} contour as a cylinder with a length of ~2.70 ± 0.20 pc and a diameter of ~0.46 ± 0.06 pc. As shown in Figure 2(a), there are several small red contours not conjunct with the main structure and that lack magnetic field segments, so we do not count them in further calculations. Also, the protostellar core MM6 has the highest $N(H_2)$ and strong $N_2H^+(J = 1 - 0)$ (Figure 3(a)) emission but lacks magnetic field segments, so we mask MM6 to avoid bias when estimating the mass and velocity dispersion as well. The mass and density are then calculated as $M \sim 868^{+116}_{-118}\, M_\odot$ and $\rho \sim 1.31 \times 10^{-19}$ g cm^{-3}, respectively, and, further, the line mass $M_l \sim 321 \pm 43\, M_\odot$ pc^{-1}. The corresponding volume density (n_{H_2}) is derived as ~2.80×10^4 cm^{-3} from $\rho = \mu_{H_2} m_H n_{H_2}$, where $\mu_{H_2} \simeq 2.8$ is the molecular weight per hydrogen molecule (J. Kauffmann et al. 2008), and m_H is the atomic mass of hydrogen.

We fit the FWHM line width, Δv, by a hyperfine structure line fitting based on Nobeyama 45 m $N_2H^+(J = 1 - 0)$ data (Figures 3(a)–(c), adopted from K. Tatematsu et al. 2021) with a resolution of 18″. The average σ_v is then derived as ~0.52 km s^{-1} from $\Delta v / \sqrt{8 \ln(2)} = \sqrt{{\sigma_{th}}^2 + {\sigma_v}^2}$, where

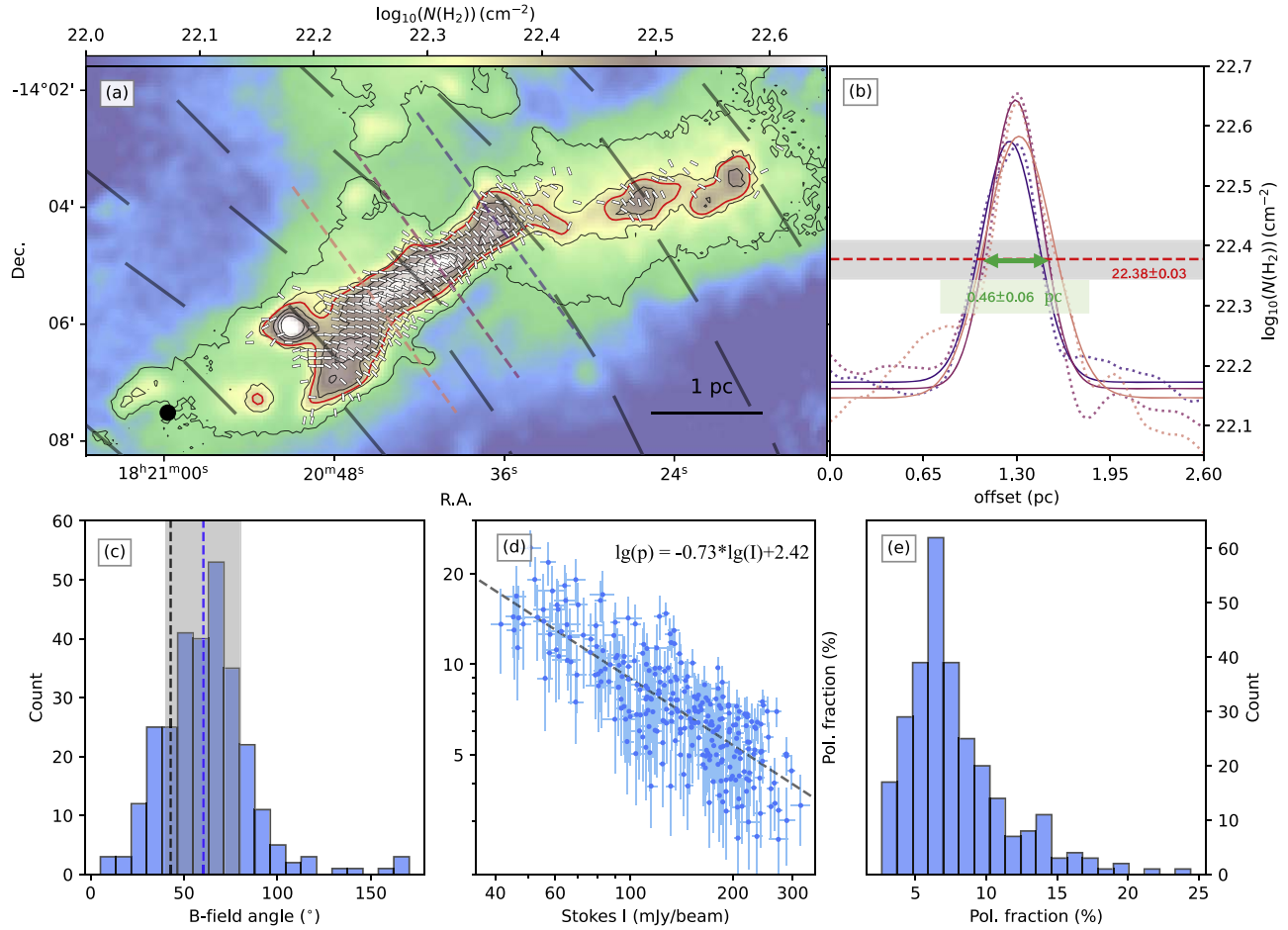

Figure 2. (a) Magnetic field orientations of G16.96+0.27 overlaid on the $N(H_2)$ map with black contours showing 850 μm Stokes I levels of [150, 200, 250, 300, 350] mJy beam^{-1}. The short white and long black segments represent the magnetic field inferred from JCMT/POL-2 850 μm observations and Planck 353 GHz data, respectively. The 14.″4 beam size and a 1 pc scale bar are shown in the left and right lower corners. The dashed lines mark the cross sections used for the $N(H_2)$ profile fitting shown in (b), and the red contours represent the average FWHM $N(H_2)$ value of $\sim$2.39 $\times$ 10^{22} cm^{-2}. (b) Gaussian fittings of $N(H_2)$ profiles from the three cross sections in (a); the offset is counted from northeast to southwest. Dashed and solid lines represent the observed data and best-fitting results, respectively. The red horizontal line marks the average FWHM $N(H_2)$, and the gray region shows the uncertainty. The green double-headed arrow shows the average FWHM value of 0.46 $\pm$ 0.06 pc. (c) Distribution of magnetic field orientations; the blue dashed line represents the average value, and the gray region marks the standard deviation range. The black dashed line marks the average value of magnetic field orientations inferred from Planck 353 GHz data. (d) Polarization fraction vs. initial Stokes I (not the combined one using the J-comb algorithm); the dashed line shows the power-law fit, and the best-fit parameters are shown in the top-right corner. (e) Distribution of polarization fraction.

$\sigma_{\rm th} = \sqrt{\frac{k_{\rm B}T}{m_{\rm N_2H^+}}}$ is the thermal velocity dispersion of N_2H^+, $k_{\rm B}$ is the Boltzmann constant, $m_{\rm N_2H^+} \sim 4.85 \times 10^{-26}$ kg is the molecular mass of N_2H^+, and T is the dust temperature (the average value is $\sim$17.4 K with a standard deviation of $\sim$0.6 K) derived when generating the $N(H_2)$ map by using the J-comb algorithm (S. Jiao et al. 2022). It is worth noting that, as shown in Figure 3(d), σ_v shows a bimodal distribution with peaks of $\sim$0.18 km s^{-1} and $\sim$0.88 km s^{-1}, and the larger ones appear in the transition areas between the two velocity peaks shown in Figure 3(b), which may be a signature of two velocity components. If so, σ_v is likely to be overestimated by a factor of 2–3. However, considering the data quality is insufficient for a deeper analysis, we still apply the average value $\sim$0.52 km s^{-1} as σ_v. This may result in an overestimation of the strength of the magnetic field in the following analyses.

We apply the Davis–Chandrasekhar–Fermi (DCF) method (L. Davis 1951; S. Chandrasekhar & E. Fermi 1953a) to estimate the magnetic field strength. The DCF method relies on the following assumptions: the turbulence is isotropic; there is equipartition between the transverse turbulent magnetic field energy and kinetic energy; and the turbulent-to-ordered ($B_{\rm t}/B_{\rm o}$) or turbulent-to-total ($B_{\rm t}/B_{\rm tot}$) magnetic field ratio can be traced by the statistics of the magnetic field orientations. Then, the ordered and total POS magnetic field strength could be estimated from

$$B_{\rm o} = f_{\rm dcf}\sqrt{4\pi\rho}\,\frac{\sigma_v}{B_{\rm t}/B_{\rm o}} \quad (1)$$

and

$$B_{\rm tot} = f_{\rm dcf}\sqrt{4\pi\rho}\,\frac{\sigma_v}{B_{\rm t}/B_{\rm tot}}, \quad (2)$$

where $f_{\rm dcf}$ is the correction factor. When the ordered magnetic field is prominent, $B_{\rm t}/B_{\rm o}$ and $B_{\rm t}/B_{\rm tot}$ are usually estimated from $B_{\rm t}/B_{\rm o} \sim B_{\rm t}/B_{\rm tot} \sim \sigma_\theta$, where σ_θ is the angular dispersion of POS magnetic field orientations.

We note that there are many versions of the DCF method showing different ways to quantify $B_{\rm t}/B_{\rm tot}$ more accurately (e.g., D. Falceta-Gonçalves et al. 2008; J. Cho & H. Yoo 2016; J. Liu et al. 2021). Here, we use two of them to estimate

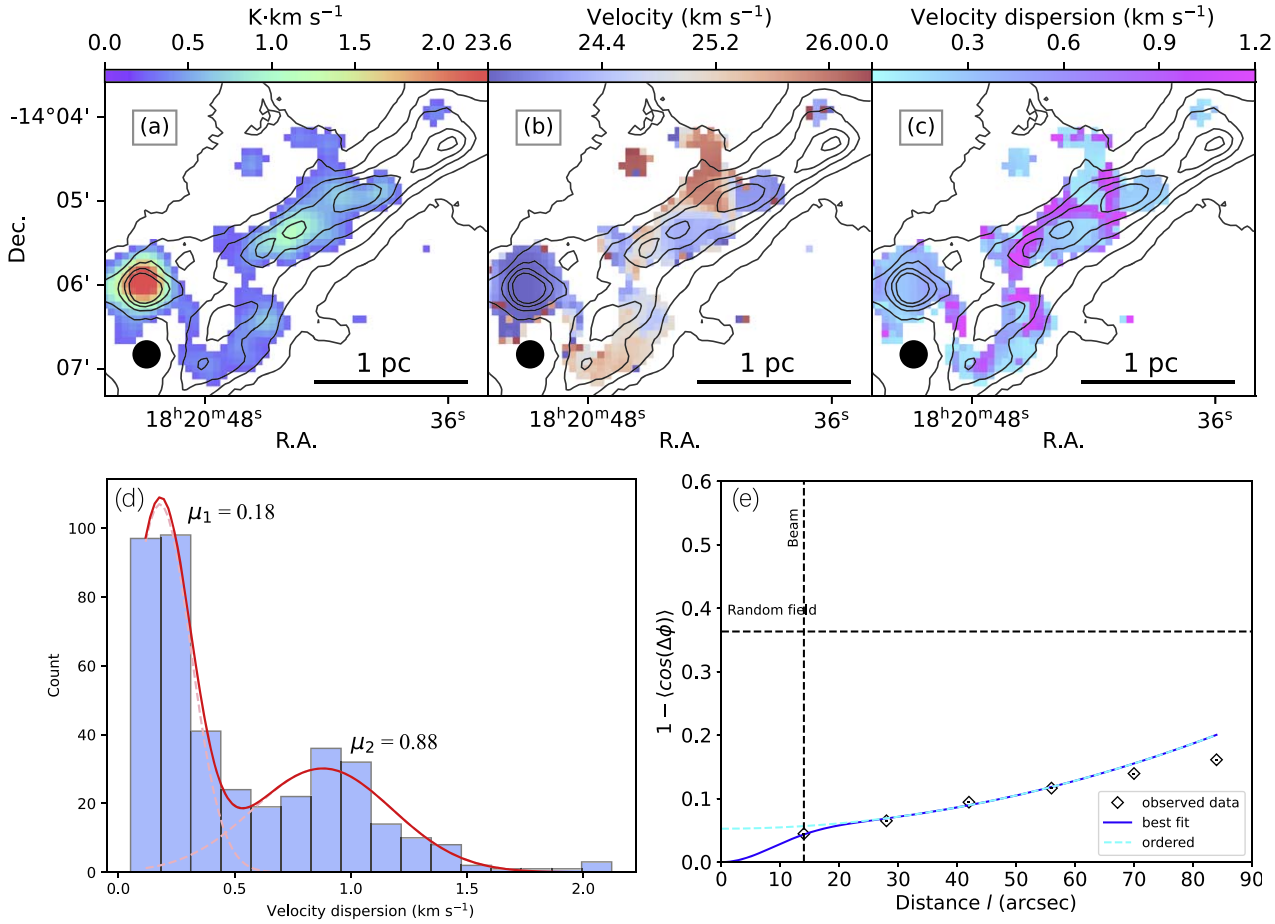

Figure 3. (a) Integrated line emission of the isolated hyperfine component of N_2H^+ with an S/N higher than 3. (b) Centroid velocity map of N_2H^+. (c) Nonthermal velocity dispersion of N_2H^+. Contours in (a)–(c) are the 850 μm Stokes I levels of [150, 200, 250, 300, 350] mJy beam^{-1}; the 18″ beam size and a 1 pc scale bar are shown in the left and right lower corners, respectively. (d) Distribution of the velocity dispersion shown in (c). The red curve shows the best fitting of the bimodal distribution with peaks of ∼0.18 km s^{-1} and ∼0.88 km s^{-1}; dashed curves represent the two single Gaussian fittings. (e) ADF of G16.96+0.27. The diamond symbols represent the observed data points. Blue and cyan lines indicate the best-fitted result and the large-scale component of the best fit, respectively. The horizontal line marks the angular dispersion function value of a random field (0.36, J. Liu et al. 2021).

the magnetic field strength for comparison and analysis: the classical DCF method (E. C. Ostriker et al. 2001) and the calibrated angular dispersion function (ADF) method (R. H. Hildebrand et al. 2009; M. Houde et al. 2009; M. Houde et al. 2016), a modified DCF method. Using the $f_{\rm dcf} = 0.5$ derived from the numerical models (E. C. Ostriker et al. 2001) and the estimated σ_θ of $20 \pm 1°$, we obtain $B_{\rm dcf} \sim 0.5\sqrt{4\pi\rho}\,\sigma_v/\sigma_\theta \sim 96 \pm 17\ \mu$G.

J. Liu et al. (2021) calibrated the ADF method and found it accounts for the ordered magnetic field structure and beam smoothing. The turbulent correlation effect is derived from

$$1 - \langle \cos[\Delta\Phi(l)] \rangle \simeq \frac{\langle B_t{}^2 \rangle}{\langle B^2 \rangle} \times (1 - e^{-l^2/2(l_\delta^2+2W^2)}) + a'_2\, l^2, \quad (3)$$

where $\Delta\Phi(l)$ is the angular difference of two magnetic field angles separated by a distance of l, l_δ is the turbulent correlation length for local turbulent magnetic field, $W = l_{\rm beam}/\sqrt{8\ln 2}$ is the standard deviation of the Gaussian beam size, and the second-order term $a'_2\, l^2$ is the first term of Taylor expansion of the ordered component of the ADF. Figure 3(e) shows the ADF of G16.96+0.27; we fit the ADF by reduced χ^2 minimization with the best-fitted $(\langle B_t{}^2\rangle/\langle B^2\rangle)^{0.5}$ of 0.23; thus, by using $B \sim 0.21\sqrt{4\pi\rho}\,\sigma_v(\langle B_t{}^2\rangle/\langle B^2\rangle)^{-0.5}$ (J. Liu et al. 2021), we obtain $B_{\rm adf} \sim 60 \pm 10\ \mu$G. Thus, we estimate an average strength of $B_{\rm pos} = 0.5(B_{\rm dcf} + B_{\rm adf}) \sim 78 \pm 20\ \mu$G for further analysis.

4. Discussion

As G16.96+0.27 has a relatively simple filamentary shape, for further analysis, we identify the skeleton of this structure by applying the FilFinder algorithm (E. W. Koch & E. W. Rosolowsky 2015) to the $N(H_2)$ map. As shown in the upper panel of Figure 4, we mask MM6 when finding the skeleton for the reasons mentioned in Section 3.

4.1. Equilibrium State

For an unmagnetized filamentary cloud, the virial mass per unit length is $M_{{\rm vir},l} = 2\sigma_{\rm tot}{}^2/G$ (J. D. Fiege & R. E. Pudritz 2000), where $\sigma_{\rm tot} = \sqrt{c_{\rm s}{}^2 + \sigma_v{}^2}$ is the total velocity dispersion, $c_{\rm s} = \sqrt{\frac{k_{\rm B}T}{\mu_p m_{\rm H}}} \simeq 0.25$ km s^{-1} is the isothermal sound speed with an average T of ∼17.4 K, and $\mu_p \simeq 2.37$ is the mean molecular weight per free particle (J. Kauffmann et al. 2008). The virial

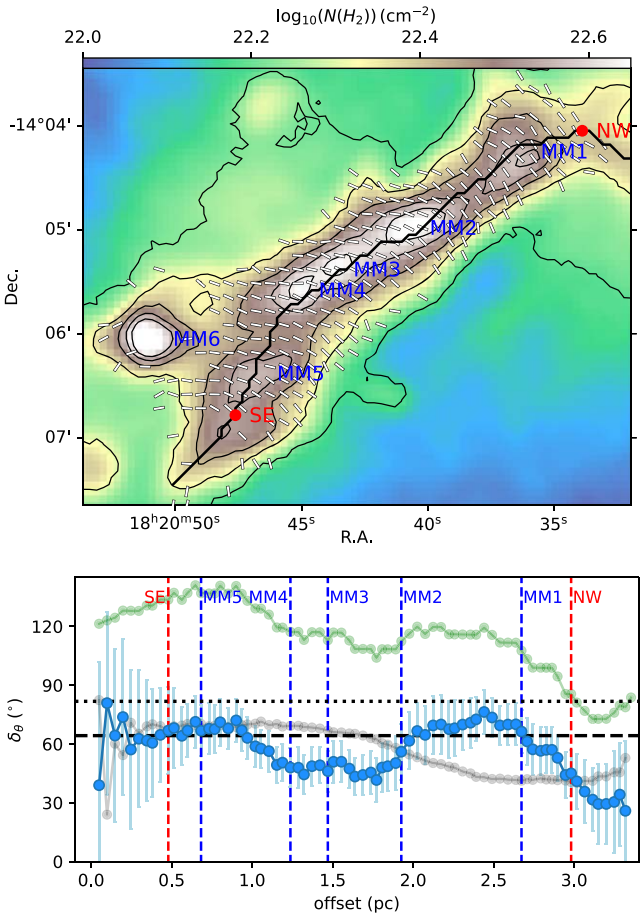

Figure 4. Upper: magnetic field orientation map overlaying the $N(H_2)$ map with contours showing 850 μm Stokes I levels of [150, 200, 250, 300, 350] mJy beam^{-1}. The black curve shows the filament skeleton derived from FilFinder. The two red points mark the two ends of the skeleton. The six fragments are marked as MM1–6. Lower: the filament skeleton and magnetic field angle difference. The blue curve shows the angle difference between the local magnetic field and the filament skeleton; the offset is counted from the southeast to the northwest of the skeleton. The gray and green curves are the magnetic field orientation and filament orientation along the skeleton, respectively. The dashed black line marks the angle difference between the mean filament skeleton orientation and the mean POL-2 magnetic field orientation, 65.7°. In contrast, the dotted black line shows the angle difference between the mean filament skeleton orientation and the mean Planck magnetic field orientation, 81.8°. The two red dashed lines mark the locations of the two endpoints in the upper panel and the five blue dashed lines mark the locations of MM1–5.

parameter is then defined as

$$\alpha_{\rm vir} = \frac{M_{{\rm vir},l}}{M_l} = \frac{2{\sigma_{\rm tot}}^2}{GM_l}; \quad (4)$$

$M_{{\rm vir},l}$ of G16.96+0.27 is $\sim 153\,M_\odot\,{\rm pc}^{-1}$, and thus $\alpha_{\rm vir} \sim 0.48 \pm 0.07$, suggesting that turbulence is weaker than gravity.

Taking the magnetic field into account, the maximum mass per length that the magnetic field can support against gravity is $M_{\Phi,l} = \Phi_l/(2\pi\sqrt{G})$, where Φ_l is the magnetic flux per unit length. The local magnetic stability critical parameter (R. M. Crutcher et al. 2004) is then defined as

$$\lambda = \frac{M_l}{M_{\Phi,l}} = \frac{\mu_{\rm H_2} m_{\rm H} N({\rm H_2})}{B/(2\pi\sqrt{G})} \simeq 7.6 \times 10^{-21} \frac{N({\rm H_2})}{B}, \quad (5)$$

where $N(H_2)$ is the column density in units of cm^{-2}, and B is the total 3D magnetic field strength in units of μG. For G16.96+0.27, the average $N(H_2)$ is $\sim(3.10 \pm 0.52) \times 10^{22}\,{\rm cm}^{-2}$ and $B_{\rm pos} \sim 78\ \mu$G, considering $B = \frac{4}{\pi}\bar{B}_{\rm pos} \sim 99\ \mu$G (R. M. Crutcher et al. 2004); λ is derived as $\sim 2.56 \pm 0.74$, indicating the magnetic field is also weaker than gravity. However, R. M. Crutcher et al. (2004) proposed that the observed M/Φ_l will be overestimated by up to a factor of 3 due to geometrical effects; this correction results in a lower limit of λ as $\lambda_{\rm min} \sim 0.86 \pm 0.25$, showing a possibility of the magnetic field being stronger than gravity at some certain inclination angles.

R. Kashiwagi & K. Tomisaka (2021) found that, when a filamentary cloud is supported by both a perpendicular magnetic field and thermal and turbulent motions, the maximum stable mass per unit length is $M_{{\rm crit},l} \simeq \sqrt{{M_{\Phi,l}}^2 + {M_{{\rm vir},l}}^2}$, which implies

$$\frac{M_l}{M_{{\rm crit},l}} = \frac{1}{\sqrt{\lambda^{-2} + \alpha_{\rm vir}^2}}. \quad (6)$$

$(M_l/M_{{\rm crit},l})$ is $\sim 1.62 \pm 0.23$, suggesting the magnetic field and turbulence together are weaker than gravity. However, the lower limit $(M_l/M_{{\rm crit},l})_{\rm min} \sim 0.79 \pm 0.20$ if applying $\lambda_{\rm min} \sim 0.86$, suggesting the magnetic field and turbulence together are stronger than gravity. Thus, a $(M_l/M_{{\rm crit},l}) \sim 1$ is more convincing, indicating G16.96+0.27 is in a quasi-equilibrium state. However, considering the magnetic field strength could be overestimated (see Section 3.2), $(M_l/M_{{\rm crit},l})$ could be even larger, and thus the filament is more likely to be a gravitationally bound system.

4.2. Fragmentation inside the Quiescent Filament

As shown in Figures 1(a)–(c), there are several possible fragments along the filament major axis, which have been identified as protostellar (MM1, MM2, and MM6) and starless (MM3, MM4, and MM5) cores (G. Kim et al. 2020; E. Mannfors et al. 2021; K. Tatematsu et al. 2021). Such fragmentation can be explained by the so-called "sausage instability" of a cylindrical gas structure (e.g., S. Chandrasekhar & E. Fermi 1953b; S.-I. Inutsuka & S. M. Miyama 1992; K. Wang et al. 2014; Y. Contreras et al. 2016). In an isothermal gas cylinder with a helicoidal magnetic field, F. Nakamura et al. (1993) predicted a typical spacing of fragments by

$$L \simeq \frac{2\pi}{0.72} H[(1+\gamma)^{1/3} - 0.6]^{-1}, \quad (7)$$

where $\gamma = {B_{\rm c}}^2/(8\pi\rho_{\rm c}\sigma^2)$, $\rho_{\rm c}$ and $B_{\rm c}$ are the density and magnetic field strength in the center, and H is the scale height. According to F. Nakamura et al. (1993), for a cylindrical gas structure with a magnetic field of $B = (0, B_\phi, B_z)$, the scale height (H) is defined from

$$4\pi G\rho_{\rm c} H^2 = \sigma^2 + \frac{{B_{\rm c}}^2}{16\pi\rho_{\rm c}}(1 + \cos^2\theta), \quad (8)$$

where $\theta = \lim_{r\to\infty} \tan^{-1} B_\phi/B_z$ denotes the ratio of B_ϕ and B_z; when $\theta = 0$, the magnetic field is parallel to the filament. $\sigma = c_{\rm s} \sim 0.25\,{\rm km\,s^{-1}}$ is the isothermal sound speed, and it is replaced by $\sigma_{\rm v} \sim 0.52\,{\rm km\,s^{-1}}$ when the fragmentation is governed by the turbulence rather than thermal Jeans instability.

In G16.96+0.27, we estimated θ as the angle between the mean POS magnetic field orientation and filament skeleton ($\sim$65.7°), and $\rho_c \sim 1.92 \times 10^{-19}\,\mathrm{g\,cm^{-3}}$ from $\rho_c = \frac{\rho n_{H_2,c}}{n_{H_2}}$, where $n_{H_2,c} \sim 4.55 \times 10^{22}\,\mathrm{cm^{-2}}$ is the column density in the center. And we assume $B_c \sim B \sim 99\,\mu$G. Therefore, we have thermal support $H_{thermal} \sim 0.04$ pc and turbulent support $H_{turbulent} \sim 0.05$ pc. Further, we have $L_{thermal}$ of $\sim$0.31 pc and $L_{turbulent}$ of $\sim$0.75 pc.

The separations between two nearby fragments are counted from center to center with an average of $\sim 0.47 \pm 0.15$ pc (range in $\sim$0.21–0.65 pc). Considering the possible effect of projection, the separations would be $2/\pi$ times the 3D ones on average (P. Sanhueza et al. 2019). And the possible 3D separations are $\sim$0.33–1.02 pc with an average of $\sim 0.74 \pm 0.23$ pc, which favors turbulent support rather than thermal support. It is worth noting that the popularly used spacing equation $L \simeq 22H$ with $H = \sigma\sqrt{4\pi G\rho_c}$ is under the condition of $\gamma = 0$ (i.e., ignorance of the magnetic field). Though Equation (7) cares about the magnetic field, it is under a helicoidal magnetic field assumption. For G16.96+0.27, we have no evidence of a helicoidal magnetic field, thus the result of L is for reference only.

4.3. Multiscale Cloud–field Alignment

As mentioned in Section 3, the $\sim$0.13 pc scale magnetic field shows rough agreement with the $\sim$2.6 pc scale one but with some discrepancies in high-density regions. For further analysis, we use the histogram of relative orientations (HROs; J. D. Soler et al. 2013, 2017) method. The HRO parameter ξ is defined as

$$\xi = \frac{A_0 - A_{90}}{A_0 + A_{90}}, \tag{9}$$

where A_0 and A_{90} represent the areas under the histogram of the Φ (the angle between the POS magnetic field orientation and the isocolumn density structure) value from 0° to 22.5° and 67.5° to 90°, respectively. While the derivation of ξ completely ignores angles from 22.5° to 67.5°, D. L. Jow et al. (2018) improved the HRO analysis with the projected Rayleigh statistic (PRS) to overcome the shortcoming. Thus, we also use the normalized version of the PRS, the alignment measure (AM) parameter (A. Lazarian et al. 2018; J. Liu et al. 2022), to study the relative alignment. The AM parameter is defined as

$$\mathrm{AM} = \langle \cos 2\delta_\theta \rangle, \tag{10}$$

where δ_θ represents the relative orientation angle between the magnetic field and gas structure. A positive value of AM and ξ means the magnetic field tends to be parallel with the $N(H_2)$ contour while a negative value stands for a perpendicular alignment.

We use POL-2 magnetic field (14.″4) data and $N(H_2)$ from the J-comb algorithm (18″) to calculate the small-scale AM and ξ. For the large-scale ones, we derive the column density by $\tau_{353}/N(H) = 1.2 \times 10^{-26}\,\mathrm{cm^{-2}}$ to match the Planck 353 GHz magnetic field data, where τ_{353} is the Planck 353 GHz dust optical depth (Planck Collaboration Int. XI et al. 2014). We mask regions with Galactic latitude lower than 0.185° to avoid the effect of the emission from the Galactic plane.

As shown in the right panel of Figure 5, AM and ξ exhibit the same behavior with increasing $N(H_2)$. They go from positive to negative at a large scale (red curve, low $N(H_2)$ traced by Planck data) but have the opposite behavior at a small scale (blue curve, high $N(H_2)$ traced by Herschel), showing a positive slope.

The behavior of AM and ξ indicates the following cloud–field alignment phenomenon. In the diffuse environment (with a $N(H_2)$ of $\sim 5.0 \times 10^{21}\,\mathrm{cm^{-2}}$, shown in light blue in the left panel of Figure 5), the magnetic field tends to be parallel with the gas structure. In the host structure (with a $N(H_2)$ of $\sim 1.3 \times 10^{22}\,\mathrm{cm^{-2}}$, shown in green in the left panel of Figure 5), the magnetic field turns to be perpendicular to the gas structure, which is perpendicular to the Galactic plane and extends to the northwest conjunct with M16, an active high-mass star-forming cloud (e.g., J. J. Hester et al. 1996; K. Sugitani et al. 2002; K. Pattle et al. 2018). In the outskirts (with a $N(H_2)$ of $\sim 2.5 \times 10^{22}\,\mathrm{cm^{-2}}$) of the main structure (the middle panel of Figure 5), the alignment keeps perpendicular as in the host structure. In the dense center (with a $N(H_2)$ higher than $\sim 3.2 \times 10^{22}\,\mathrm{cm^{-2}}$), it becomes $\sim$45° and shows a possible trend to be closer to parallelism.

Along the filament, we average the magnetic field orientation and skeleton orientation using a 32″ filter, as 32″($\sim$0.29 pc) is similar to the diameter of the filament, and calculate δ_θ between them. As shown in the lower panel of Figure 4, regions beyond SE and NW points have few magnetic field segments and substantial uncertainties on δ_θ, so we mainly discuss the skeleton in between. δ_θ shows fluctuations along the skeleton; it is $\sim$65°–80° at both ends, but becomes $\sim$40°–50° at the center. The behavior of δ_θ indicates that the local magnetic field tends to be perpendicular to the filament at the two diffuse ends but shows a trend to have a smaller offset with the filament at the dense center, which agrees with the behavior of AM and ξ shown in Figure 5.

T. G. S. Pillai et al. (2020) found a similar positive slope of ξ in dense regions of the hub-filament system Serpens South, suggesting the gas filaments are merging into the central hub and reorienting the magnetic field in the dense gas flows. W. Kwon et al. (2022) found that the ξ of Serpens Main shows large fluctuations with increasing $N(H_2)$, which is interpreted as the density gradient along the elongated structures becoming significant and the magnetic field being dragged along with the increasing density. Furthermore, in the massive IRDC G28.34 (the Dragon cloud), J. Liu et al. (2024) found that the AM parameter also goes from negative to positive with increasing $N(H_2)$, and fluctuates around 0 in the very dense region traced by Atacama Large Millimeter/submillimeter Array (ALMA), suggesting G28.34 is located in a trans-to-sub-Alfvénic environment.

However, compared to Serpens South, Serpens Main, and G28.34, G16.96+0.27 has a much simpler structure and less star formation activity. As shown in the upper panel of Figure 1, MM1 and MM6 are not connected with the main structure from the infrared view, and most of the rest (MM3–MM5) are still starless cores. All the fragments have an average POS separation of $\sim$0.47 pc, which may favor turbulent-supported rather than thermal-supported fragmentation (see the discussion in Section 4.2). These results may indicate the following phenomenon: the G16.96+0.27 filament as a whole is quiescent and in quasi-equilibrium, as reflected by the dark infrared morphology shown in Figure 1 and the $M_l/M_{crit,l}$ value. However, in the center region, the star formation process may have already begun, as reflected by the fragments shown

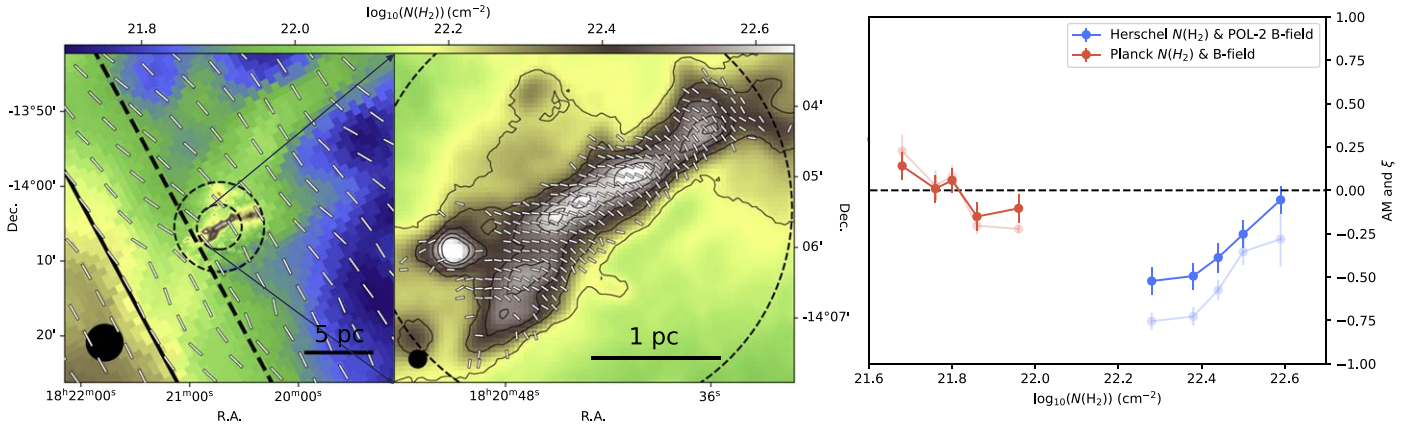

Figure 5. Left: column density inferred from Planck dust optical depth map at 353 GHz (τ_{353}) overlaid with the one (within the outer black dashed circle) inferred from Herschel data by using the J-comb algorithm (S. Jiao et al. 2022). The segments show the magnetic fields derived from Planck 353 GHz polarization data; the black circle shows the beam of Planck 353 GHz data with a resolution of 4.′8, and the black solid line and dashed line represent 0° and 0.185° Galactic latitude, respectively. The two dashed circles mark the central regions of 12′ and 6′ radius, respectively. A 5 pc scale bar is shown in the lower-right corner. Middle: column density inferred from Herschel data by using the J-comb algorithm with a resolution of 18″ (the beam is shown in the lower-left corner); overlaid segments represent the magnetic field orientation inferred from JCMT/POL-2 850 μm polarization data. The dashed circle marks the central 6′ region, which has a useful level of coverage in the POL-2 observations. The contours show the 850 μm Stokes I levels of [150, 200, 250, 300, 350] mJy beam^{-1}. A 1 pc scale bar is shown in the lower-right corner. Right: alignment measure parameter AM and HRO parameter ξ calculated for the different $N(H_2)$ bins in G16.96+0.27. Red data points show the AM values (light red for ξ) inferred from Planck 353 GHz data, and the blue ones show the AM values (light blue for ξ) inferred from the Herschel $N(H_2)$ and POL-2 magnetic field.

in Figure 1 and the discussion in Section 4.2. Thus, gravity has overcome the support of the magnetic field and turbulence, and dragged the field lines to align with the filament structure, as has been observed at smaller scales in different targets (e.g., P. Sanhueza et al. 2021; P. C. Cortes et al. 2024). Further, higher-resolution observations toward the center region are needed to investigate whether AM and ξ would fluctuate around 0 like G28.34 (J. Liu et al. 2024) or turn around, showing the decreasing trend seen in the very dense regions ($N(H_2) \geqslant 1.6 \times 10^{23}$ cm^{-2}) in Serpens Main (W. Kwon et al. 2022).

5. Summary

In this paper, we have presented JCMT/POL-2 polarization observations toward an IRDC, G16.96+0.27, and the main conclusions are as follows:

(1) The average magnetic field orientation traced by JCMT/POL-2 is ∼60°, and a significant number of magnetic field segments exhibit a perpendicular alignment with the filament structure of G16.96+0.27, with an average angle difference of ∼66°. This result is consistent with the larger-scale magnetic field orientations traced by Planck 353 GHz data. The POS magnetic field strength is estimated to be $B_{\rm pos,dcf} \sim 96\ \mu$G and $B_{\rm pos,adf} \sim 60\ \mu$G using the classical DCF method and the ADF method, with an average strength of ∼78 μG.

(2) The virial parameter and magnetic stability critical parameter are calculated as $\alpha_{\rm vir} \sim 0.48$ and $\lambda \sim 2.56$ with $\lambda_{\rm min} \sim 0.86$, respectively. And the estimated $(M_l/M_{{\rm critc},l})$ is ∼1, indicating that G16.96+0.27 is in a quasi-equilibrium state, but is more likely to be in a gravitationally bound state when considering the magnetic field could be overestimated.

(3) We calculate the HRO parameter ξ and the AM parameter based on Planck and JCMT data to study multiscale cloud–field alignment. With increasing $N(H_2)$, they first go across 0 to a negative minimum and then move back to 0. Along the filament, we apply the FilFinder algorithm to identify the skeleton of G16.96+0.27 and find that the local cloud–field alignment varies along the filament. The alignment is perpendicular at both diffuse ends but turns to be ∼45° at the dense center, which is consistent with the behavior of AM and ξ. We also find that the observed separations among the fragments are in agreement with the predicted spacing from the "sausage instability" theory under the turbulent support assumption (Section 4.2). These results may reflect that, although G16.96+0.27 is in quasi-equilibrium overall, fragmentation has already begun in the center of the filament, and such a phenomenon of cloud–field alignment inside IRDCs may be a possible sign of an early stage of star formation activity.

Acknowledgments

This work has been supported by the National Key R&D Program of China (No. 2022YFA1603100), the Shanghai Rising-Star Program (23YF1455600), and the Natural Science Foundation of Shanghai (No. 23ZR1482100). T.L. acknowledges support from the National Natural Science Foundation of China (NSFC) through grants No. 12073061 and No. 12122307, the Tianchi Talent Program of Xinjiang Uygur Autonomous Region, and the international partnership program of the Chinese Academy of Sciences through grant No. 114231KYSB20200009. X.L. acknowledges support from the NSFC through grant Nos. 12273090 and 12322305, and the Chinese Academy of Sciences (CAS) "Light of West China" Program No. xbzg-zdsys-202212. M.J. acknowledges the support of the Research Council of Finland grant No. 348342. C.W.L. acknowledges support from the Basic Science Research Program through the NRF funded by the Ministry of Education, Science, and Technology (NRF-2019R1A2C1010851) and by the Korea Astronomy and Space Science Institute grant funded by the Korea government (MSIT; project No. 2024-1-841-00). W.K. was supported by the National Research Foundation of

Korea (NRF) grant funded by the Korea government (MSIT; project No. RS-2024-00342488). K.P. is a Royal Society University Research Fellow, supported by grant number URF\R1\211322. P.S. was partially supported by a Grant-in-Aid for Scientific Research (KAKENHI Number JP22H01271 and JP23H01221) of JSPS.

The James Clerk Maxwell Telescope is operated by the East Asian Observatory on behalf of The National Astronomical Observatory of Japan; Academia Sinica Institute of Astronomy and Astrophysics; the Korea Astronomy and Space Science Institute; the National Astronomical Research Institute of Thailand; Center for Astronomical Mega-Science (as well as the National Key R&D Program of China with No. 2017YFA0402700). Additional funding support is provided by the Science and Technology Facilities Council of the United Kingdom and participating universities and organizations in the United Kingdom and Canada. Additional funds for the construction of SCUBA-2 were provided by the Canada Foundation for Innovation.

Software: Astropy (Astropy Collaboration et al. 2013, 2018), FilFinder (E. W. Koch & E. W. Rosolowsky 2015).

Appendix A
Data Reduction Procedures of JCMT/POL-2 Data

As the polarization fraction is forced to be positive, a bias is thus introduced (J. E. Vaillancourt 2006), and the therefore debiased polarized intensity (PI) and corresponding uncertainty (δ_{PI}) are calculated from

$$PI = \sqrt{Q^2 + U^2 - 0.5(\delta_Q{}^2 + \delta_U{}^2)} \tag{A1}$$

and

$$\delta_{PI} = \sqrt{\frac{Q^2\delta_Q{}^2 + U^2\delta_U{}^2}{Q^2 + U^2}}, \tag{A2}$$

where δ_Q and δ_U are the uncertainties of Q and U. The debiased polarization fraction (p) and corresponding uncertainty (δ_p) are then derived by

$$p = PI/I \tag{A3}$$

and

$$\delta_p = \sqrt{\frac{\delta_{PI}{}^2}{I^2} + \frac{PI^2\delta_I{}^2}{I^4}}, \tag{A4}$$

where δ_I is the uncertainty of I. Next, the polarization angle (θ) and corresponding uncertainty (δ_θ) are calculated (J. Naghizadeh-Khouei & D. Clarke 1993) from

$$\theta = 0.5\tan^{-1}(U/Q) \tag{A5}$$

and

$$\delta_\theta = \frac{1}{2}\sqrt{\frac{Q^2\delta_U{}^2 + U^2\delta_Q{}^2}{(Q^2 + U^2)^2}}. \tag{A6}$$

Appendix B
J-comb Algorithm

We get the column density map by applying the J-comb algorithm (S. Jiao et al. 2022) based on level 2.5 processed archival Herschel data and this JCMT 850 μm data; the main procedures are as follows: 1. derive the combined Stokes I map. We extrapolated an 850 μm flux map from the spectral energy distribution (SED) of Herschel 250/350/500 μm data using the Spectral and Photometric Imaging REceiver (SPIRE; obsID: 1342228342; M. J. Griffin et al. 2010). Taking this map as a model image, we deconvolved the Planck 353 GHz map (Planck Collaboration Int. XIX et al. 2011) with the Lucy–Richardson algorithm (L. B. Lucy 1974). The obtained deconvolved map has an angular resolution close to the SPIRE 500 μm data and preserves the flux level of the initial Planck map. Then, the combined Stokes I map (as shown in Figure 1(a)) was generated via the J-comb algorithm (S. Jiao et al. 2022) by combining the deconvolved map with the JCMT 850 μm Stokes I map in the Fourier domain. 2. SED fitting. We smoothed the Herschel images at 70/160 μm using the Photodetector Array Camera and Spectrometer (obsID: 1342228372; A. Poglitsch et al. 2010), SPIRE 250 μm, and the combined JCMT 850 μm Stokes I map to a common angular resolution of the largest beam. We weighted the data points by the measured noise level in the least-squares fits. As a modified blackbody assumption, the flux density S_ν at the frequency ν is given by

$$S_\nu = \Omega_m B_\nu(T)(1 - e^{-\tau_\nu}), \tag{B1}$$

where Ω_m is the solid angle, and $B_\nu(T)$ is the Planck function at temperature $T_{\rm dust}$. Then the column density is derived from

$$N(\mathrm{H_2}) = \tau_\nu/\kappa_\nu\mu m_{\rm H}, \tag{B2}$$

where $\kappa_\nu = 0.1\mathrm{cm^2\,g^{-1}}(\nu/1000\,\mathrm{GHz})^\beta$ is the dust opacity assuming a gas-to-dust ratio of 100 and an opacity index β of 2 (R. H. Hildebrand 1983; S. V. W. Beckwith et al. 1990), $\mu = 2.8$ is the molecular weight per hydrogen molecule (J. Kauffmann et al. 2008), and $m_{\rm H}$ is the atomic mass of hydrogen.

ORCID iDs

Qi-Lao Gu (顾琦烙) https://orcid.org/0000-0002-2826-1902
Tie Liu (刘铁) https://orcid.org/0000-0002-5286-2564
Zhi-Qiang Shen (沈志强) https://orcid.org/0000-0003-3540-8746
Julien Montillaud https://orcid.org/0000-0001-7032-632X
Mika Juvela https://orcid.org/0000-0002-5809-4834
Xing Lu (吕行) https://orcid.org/0000-0003-2619-9305
Chang Won Lee https://orcid.org/0000-0002-3179-6334
Junhao Liu (刘峻豪) https://orcid.org/0000-0002-4774-2998
Pak Shing Li https://orcid.org/0000-0001-8077-7095
Xunchuan Liu (刘训川) https://orcid.org/0000-0001-8315-4248
Doug Johnstone https://orcid.org/0000-0002-6773-459X
Woojin Kwon https://orcid.org/0000-0003-4022-4132
Kee-Tae Kim https://orcid.org/0000-0003-2412-7092
Ken'ichi Tatematsu https://orcid.org/0000-0002-8149-8546
Patricio Sanhueza https://orcid.org/0000-0002-7125-7685
Patrick Koch https://orcid.org/0000-0003-2777-5861
Qizhou Zhang https://orcid.org/0000-0003-2384-6589
Kate Pattle https://orcid.org/0000-0002-8557-3582
Naomi Hirano https://orcid.org/0000-0001-9304-7884
Dana Alina https://orcid.org/0000-0001-5403-356X
James Di Francesco https://orcid.org/0000-0002-9289-2450

References

André, P., Di Francesco, J., Ward-Thompson, D., et al. 2014, in Protostars and Planets VI, ed. H. Beuther et al. (Tucson, AZ: Univ. of Arizona Press), 27
André, P., Men'shchikov, A., Bontemps, S., et al. 2010, A&A, 518, L102
Arzoumanian, D., André, P., Didelon, P., et al. 2011, A&A, 529, L6

Astropy Collaboration, Price-Whelan, A. M., Sipőcz, B. M., et al. 2018, AJ, 156, 123
Astropy Collaboration, Robitaille, T. P., Tollerud, E. J., et al. 2013, A&A, 558, A33
Beckwith, S. V. W., Sargent, A. I., Chini, R. S., & Guesten, R. 1990, AJ, 99, 924
Chandrasekhar, S., & Fermi, E. 1953a, ApJ, 118, 113
Chandrasekhar, S., & Fermi, E. 1953b, ApJ, 118, 116
Chapin, E. L., Berry, D. S., Gibb, A. G., et al. 2013, MNRAS, 430, 2545
Ching, T.-C., Qiu, K., Li, D., et al. 2022, ApJ, 941, 122
Cho, J., & Yoo, H. 2016, ApJ, 821, 21
Contreras, Y., Garay, G., Rathborne, J. M., & Sanhueza, P. 2016, MNRAS, 456, 2041
Cortes, P. C., Girart, J. M., Sanhueza, P., et al. 2024, ApJ, 972, 115
Crutcher, R. M. 2012, ARA&A, 50, 29
Crutcher, R. M., Nutter, D. J., Ward-Thompson, D., & Kirk, J. M. 2004, ApJ, 600, 279
Currie, M. J., Berry, D. S., Jenness, T., et al. 2014, in ASP Conf. Ser. 485, Astronomical Data Analysis Software and Systems XXIII, ed. N. Manset & P. Forshay (San Francisco, CA: ASP), 391
Davis, L. 1951, PhRv, 81, 890
Falceta-Gonçalves, D., Lazarian, A., & Kowal, G. 2008, ApJ, 679, 537
Fiege, J. D., & Pudritz, R. E. 2000, MNRAS, 311, 105
Friberg, P., Bastien, P., Berry, D., et al. 2016, Proc. SPIE, 9914, 991403
Friberg, P., Berry, D., Savini, G., et al. 2018, Proc. SPIE, 10708, 107083M
Griffin, M. J., Abergel, A., Abreu, A., et al. 2010, A&A, 518, L3
Gu, Q.-L., Liu, T., Li, P. S., et al. 2024, ApJ, 963, 126
Hester, J. J., Scowen, P. A., Sankrit, R., et al. 1996, AJ, 111, 2349
Hildebrand, R. H. 1983, QJRAS, 24, 267
Hildebrand, R. H., Kirby, L., Dotson, J. L., Houde, M., & Vaillancourt, J. E. 2009, ApJ, 696, 567
Holland, W. S., Bintley, D., Chapin, E. L., et al. 2013, MNRAS, 430, 2513
Houde, M., Hull, C. L. H., Plambeck, R. L., Vaillancourt, J. E., & Hildebrand, R. H. 2016, ApJ, 820, 38
Houde, M., Vaillancourt, J. E., Hildebrand, R. H., Chitsazzadeh, S., & Kirby, L. 2009, ApJ, 706, 1504
Inutsuka, S.-I., & Miyama, S. M. 1992, ApJ, 388, 392
Jiao, S., Lin, Y., Shui, X., et al. 2022, SCPMA, 65, 299511
Jow, D. L., Hill, R., Scott, D., et al. 2018, MNRAS, 474, 1018
Kashiwagi, R., & Tomisaka, K. 2021, ApJ, 911, 106
Kauffmann, J., Bertoldi, F., Bourke, T. L., Evans, N. J. I., & Lee, C. W. 2008, A&A, 487, 993
Kim, G., Tatematsu, K., Liu, T., et al. 2020, ApJS, 249, 33
Koch, E. W., & Rosolowsky, E. W. 2015, MNRAS, 452, 3435
Könyves, V., André, P., Men'shchikov, A., et al. 2015, A&A, 584, A91
Kwon, W., Pattle, K., Sadavoy, S., et al. 2022, ApJ, 926, 163
Lazarian, A. 2003, JQSRT, 79, 881
Lazarian, A., Yuen, K. H., Ho, K. W., et al. 2018, ApJ, 865, 46
Li, H. B., Goodman, A., Sridharan, T. K., et al. 2014, in Protostars and Planets VI, ed. H. Beuther et al., 101
Li, H.-B., Yuen, K. H., Otto, F., et al. 2015, Natur, 520, 518
Li, P. S., & Klein, R. I. 2019, MNRAS, 485, 4509
Liu, H. B., Jiménez-Serra, I., Ho, P. T. P., et al. 2012, ApJ, 756, 10
Liu, J., Qiu, K., & Zhang, Q. 2022, ApJ, 925, 30
Liu, J., Zhang, Q., Commerçon, B., et al. 2021, ApJ, 919, 79
Liu, J., Zhang, Q., Lin, Y., et al. 2024, ApJ, 966, 120
Liu, T., Kim, K.-T., Juvela, M., et al. 2018b, ApJS, 234, 28
Liu, T., Li, P. S., Juvela, M., et al. 2018a, ApJ, 859, 151
Lu, X., Zhang, Q., Liu, H. B., et al. 2018, ApJ, 855, 9
Lucy, L. B. 1974, AJ, 79, 745
Mairs, S., Dempsey, J. T., Bell, G. S., et al. 2021, AJ, 162, 191
Mannfors, E., Juvela, M., Bronfman, L., et al. 2021, A&A, 654, A123
Morii, K., Sanhueza, P., Nakamura, F., et al. 2023, ApJ, 950, 148
Myers, P. C. 2009, ApJ, 700, 1609
Naghizadeh-Khouei, J., & Clarke, D. 1993, A&A, 274, 968
Nakamura, F., Hanawa, T., & Nakano, T. 1993, PASJ, 45, 551
Ostriker, E. C., Stone, J. M., & Gammie, C. F. 2001, ApJ, 546, 980
Pattle, K., Fissel, L., Tahani, M., Liu, T., & Ntormousi, E. 2023, in ASP Conf. Ser. 534, Protostars and Planets VII, ed. S. Inutsuka et al. (San Francisco, CA: ASP), 193
Pattle, K., Ward-Thompson, D., Hasegawa, T., et al. 2018, ApJL, 860, L6
Pillai, T. G. S., Clemens, D. P., Reissl, S., et al. 2020, NatAs, 4, 1195
Planck Collaboration Int. XI, Abergel, A., Ade, P. A. R., et al. 2014, A&A, 571, A11
Planck Collaboration Int. XIX, Ade, P. A. R., Aghanim, N., et al. 2011, A&A, 536, A19
Planck Collaboration Int. XXXV, Ade, P. A. R., Aghanim, N., et al. 2016, A&A, 586, A138
Poglitsch, A., Waelkens, C., Geis, N., et al. 2010, A&A, 518, L2
Sanhueza, P., Contreras, Y., Wu, B., et al. 2019, ApJ, 886, 102
Sanhueza, P., Girart, J. M., Padovani, M., et al. 2021, ApJL, 915, L10
Soam, A., Liu, T., Andersson, B. G., et al. 2019, ApJ, 883, 95
Soler, J. D., Ade, P. A. R., Angilè, F. E., et al. 2017, A&A, 603, A64
Soler, J. D., Hennebelle, P., Martin, P. G., et al. 2013, ApJ, 774, 128
Sugitani, K., Tamura, M., Nakajima, Y., et al. 2002, ApJL, 565, L25
Tafalla, M., & Hacar, A. 2015, A&A, 574, A104
Tang, Y.-W., Koch, P. M., Peretto, N., et al. 2019, ApJ, 878, 10
Tatematsu, K., Kim, G., Liu, T., et al. 2021, ApJS, 256, 25
Vaillancourt, J. E. 2006, PASP, 118, 1340
Wang, K., Zhang, Q., Testi, L., et al. 2014, MNRAS, 439, 3275
Zhang, Q., Wang, Y., Pillai, T., & Rathborne, J. 2009, ApJ, 696, 268